

PdO self-assembly on zeolite SSZ-13 with rows of $\text{O}_3\text{Al}^{+3}(\text{IV})\text{OH}_{\text{bridging}}$ selectively incorporated in PdO(101) facets for moisture-resistant methane oxidation

Libor Kovarik^{a†*}, Nicholas R. Jaegers,^a Janos Szanyi,^{a*} Mirosław A. Derewinski,^{a,b} Yong Wang^{a,c*} and Konstantin Khivantsev^{a†*}

[a] Dr. Konstantin Khivantsev, Dr. Nicholas R. Jaegers, Dr. Mirosław A. Derewinski, Dr. Janos Szanyi, Dr. Yong Wang, Dr. Libor Kovarik
Institute for Integrated Catalysis
Pacific Northwest National Laboratory
Richland, WA 99352 USA
Emails (correspondence to): Konstantin.Khivantsev@pnnl.gov, Janos.Szanyi@pnnl.gov, Yong.Wang@pnnl.gov, Libor.Kovarik@pnnl.gov

[b] Dr. Mirosław A. Derewinski, Jerzy Haber Institute of Catalysis and Surface Chemistry Polish Academy of Sciences, Krakow, Poland PL-30239

[b] Dr. Yong Wang, Voiland School of Chemical Engineering and Bioengineering
Washington State University
Pullman, WA 99164 USA

Supporting information for this article is given via a link at the end of the document; [†] These authors contributed equally

Abstract: We describe an efficient way to prepare moisture-tolerant methane (hydrocarbon) combustion catalysts based on PdO nanoparticles supported on siliceous SSZ-13 zeolite. Only zeolites with high Si/Al ratios >15 are hydrophobic enough to exclude the Pd from the micropores while forming well-faceted PdO nanoparticles. Simultaneously, during self-assembly mobile Al hydroxo species get incorporated into the as-formed PdO nanoparticles. For the first time, we reveal selective incorporation of rows of $\text{O}_3\text{Al}(\text{IV})\text{-OH}_{\text{bridging}}$ aluminum hydroxo-species into the (101) facets of PdO nanoparticles that form during thermal self-assembly in Pd/SSZ-13 using state-of-the-art atomically-resolved HAADF-STEM imaging, solid-state NMR, DFT calculations and reactivity measurements. The $\text{Al}^{+3}\text{-OH}$ moieties form atom-thin rows in place of tri-coordinate Pd ions Pd^{+2} in Pd_4O_3 on (101) facets: these tri-coordinate $\text{Pd}_4^{+2}\text{O}_3$ are responsible for C-H bond dissociation of methane and hydrocarbons during catalytic methane oxidation. However, on unmodified or non-zeolite supported PdO nanoparticles in the presence of water vapor from engine exhaust, water competes with methane by forming a deactivated $\text{Pd}_{\text{tetra}}(\text{OH})(\text{H}_2\text{O})\text{Pd}_{\text{tetra}}$ site with two water molecules on contiguous 3-coordinate Pd, which is not active for C-H bond activation. When Al-OH moieties are present in place of some tri-coordinate Pd_4O_3 sites, water dissociation becomes kinetically unfavorable due to disruption of $\text{Pd}_{\text{tetra}}(\text{OH})(\text{H}_2\text{O})\text{Pd}_{\text{tetra}}$ species formation. Consequently, our catalytic measurements reveal a significantly more stable performance of such catalysts in methane combustion in the presence of water vapor. Our findings provide an unprecedented atomic-level insight into structure-property relationships for supported PdO materials in catalytic methane oxidation and offer a new strategy to prepare moisture-tolerant Pd-containing methane combustion catalysts for green-house gas mitigation by selectively doping atomically thin rows of non-precious metal into specific facets of PdO.

Removal of toxic and greenhouse gases from air is the frontier of the environmental and emission control catalysis [1-8]. For example, NO_x and CO emissions are regulated, and a lot of progress has been achieved since 1960s to decrease their emissions from stationary and mobile sources. More specifically, catalytic converters, three-way catalysts (TWC) and selective

catalytic reduction (SCR) technology have been deployed commercially to significantly decrease emissions of CO and NO_x gases for gasoline and diesel engines [1-10]. Methane emitted by vehicles remains largely unregulated. However, the green house potential of methane alone is ~25 times higher than of carbon dioxide [11-20]. Considering also that there is a current industrial push to introduce more efficient and environmentally clean natural gas vehicles (NGVs) that operate under lean conditions, it becomes obvious that effective catalysts are needed that would provide stable methane combustion performance at relatively low temperatures (<450 °C). Current state-of-the-art technology for methane oxidation relies on palladium oxide nanoparticles [11,12]. Good agreement has been achieved in recent years considering the active phases and nanoparticle sizes. It was determined that some optimal (not too small, >10 nm) size of PdO nanoparticles is required to effectively catalyze methane and hydrocarbon combustion in the studies by Chin and co-workers [21-24]. Moreover, XPS and DFT single-crystal studies of Weaver and co-workers [24-32] unambiguously identified that PdO (101) facet, containing coordinatively unsaturated tri-coordinate $\text{Pd}(\text{II})_3\text{O}_3$ sites, is critical in inducing catalytic activity for both alkane and methane combustion. These particular tri-coordinate $\text{Pd}(\text{II})$ sites are able to form a σ -complex with methane: formation of such a complex creates a pre-requisite site with close geometric proximity between CH_4 and PdO required for further heterolytic activation of methane C-H bond on the Pd-O pair, the latter representing the rate-determining step of methane combustion. PdO (100) surface was shown to be largely inactive by the same authors. Since the first step of methane activation involves the formation of a sigma-complex on 3-coordinate Pd sites present only on (101) facets with the following (rate-determining) heterolytic cleavage of C-H bond on Pd-O pair [21-32], it is thus not surprising that larger particles with well-defined facets are more active for methane combustion. However, the main issue of supported and unsupported PdO nanoparticles is their deactivation in the presence of water vapor (always present in >2-3% in the vehicle exhaust) [11-20]. Water is believed to compete with methane for the active site whereupon water dissociates forming a catalytically inactive Pd-OH moiety. At temperatures higher than >450-500 °C water desorbs from Pd-

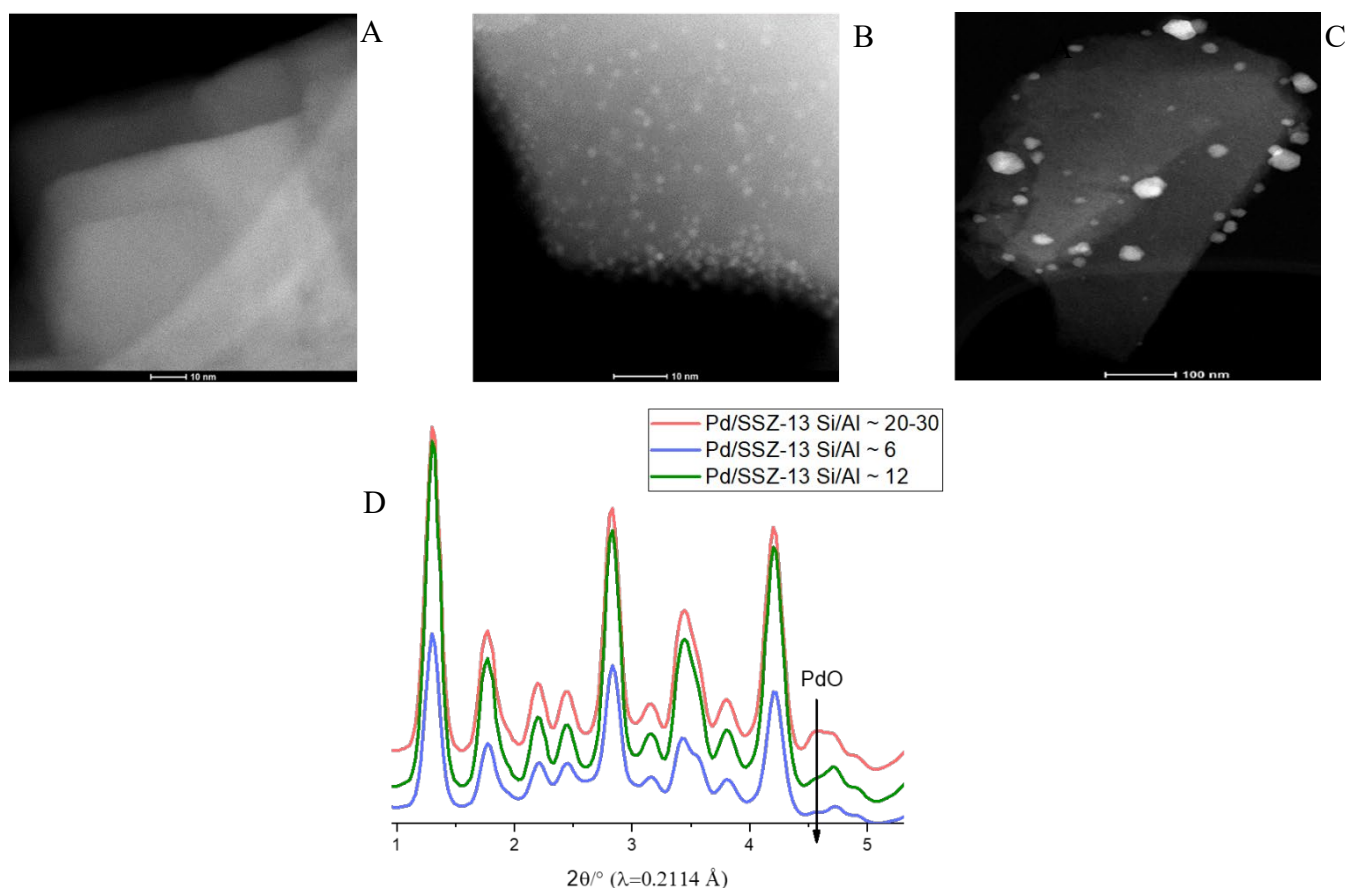


Figure 1. Representative HAADF-STEM images of 1 wt% Pd supported on H-SSZ-13 with Si/Al ~ A) 6 B) 12 C) 20-30. D) High-energy synchrotron cryo-XRD data for samples A-C. Note that in this case $\lambda=0.2114 \text{ \AA}$ (from Mo-source) and the spectrum appears „compressed“ along the x-axis.

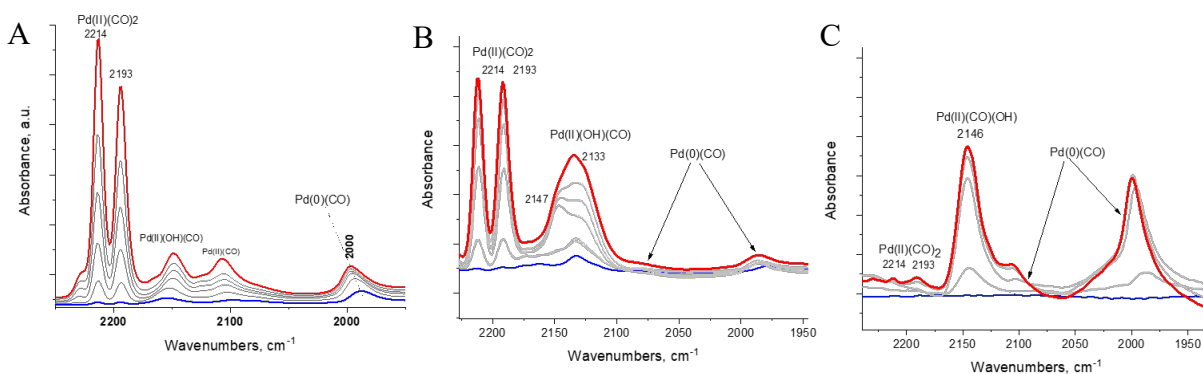


Figure 2. FTIR data during 2 Torr CO adsorption on 1 wt% Pd SSZ-13 with Si/Al ~ 6(A), 10-12 (B), 20-30 (C).

OH and -OH moieties, restoring the active Pd_4O_3 site and methane activation can proceed without much influence from the steam. However, at temperatures below, PdO materials quickly deactivate in the presence of steam [11-20]. Recent studies showed that PdO supported on zeolites exhibit improved stability in the presence of water vapor relative to typical PdO/alumina [33,34]. The reasons behind that phenomenon remain not fully understood. Hydrophobicity of zeolite was suggested to be a factor. Herein, we chose to investigate the PdO supported on SSZ-13 zeolite since SSZ-13 is one of the most hydrothermally stable zeolites known, it is used commercially for vehicle

emissions control (Cu/SSZ-13 is the commercial SCR system) [3-5] and based on the available gas adsorption studies it has low adsorption capacity for methane, especially in the presence of other gases like water, carbon dioxide and propane [35]. For example, at methane partial pressure of 0.11 kPa (corresponding to ~1,000 ppm methane in an atmospheric gas mixture) at 100 °C, SSZ-13 adsorption capacity for methane is essentially 0 [35]. Thus, majority of activity for methane combustion at temperatures of interest will come from PdO located outside zeolite, thus excluding the effect of Pd sites located in the pores.

To this end, we prepared 1 wt% Pd on SSZ-13 with varying Si/Al

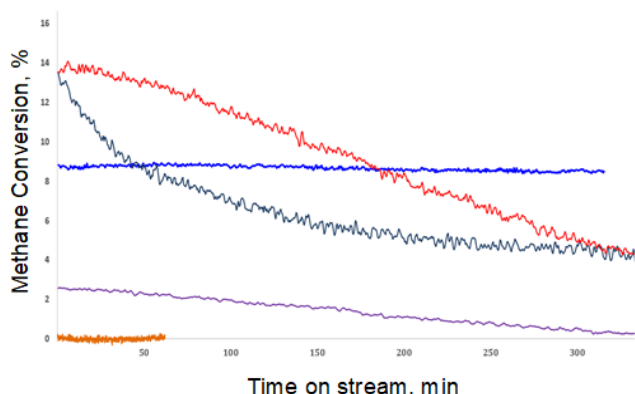


Figure 3. Methane conversion(%) vs. time-on-stream (minutes) profile for 1wt% Pd on SSZ-13 with Si/Al 6(brown), 12(purple), 30 (vibrant blue), 1wt% Pd on gamma-alumina (dull blue), and PdO nanoparticles (red). Conditions: 120 mg catalyst (in case of unsupported PdO ~1.3 mg of PdO nanoparticles were physically mixed mixed with low-surface-area high-purity corundum powder and loaded into the reactor) , 850 ppm methane, 12% O₂, ~3 % H₂O in N₂, total flow rate 300 sscm/min (GHSV ~ 150 L/g*hr). T=390 °C

ratios ~6, 10-12 and ~20-30. FTIR data (Fig. 2A-C) during CO adsorption on all samples indicates that in the sample with 1 wt% Pd/SSZ-13 with Si/Al ~ 6, Pd is dispersed selectively as isolated Pd(II)/2 Al ions (also confirmed by HAADF-STEM image in Fig. 1 and additional HAADF-STEM images for Pd/SSZ-13 samples in Fig.S1-S3). Super-electrophilic nature of a metal fragment in zeolite was identified for the first time very recently [8,36-37]. Pd/SSZ-13 with Si/Al ~ 10-12 contains predominantly atomically dispersed Pd as a mixture of Pd(II)/2Al and Pd(II)-OH/1Al sites as evidenced by FTIR measurements with CO probe molecule. In this sample, about ~15 % of Pd dispersed as small PdO clusters on the external surfaces of PdO, as evidenced by HAADF-STEM imaging and quantified by NO adsorption studies [8] (Fig. 1). For 1wt% Pd/SSZ-13 with Si/Al ~30, majority of Pd

(~70%) is present as well-defined crystalline PdO nanoparticles on the external surface of SSZ-13 further consistent with synchrotron XRD and FTIR data in Fig. 1D and Fig. 2C. As we have previously shown, the reason for the preferential exclusion of Pd from the micropores at high Si/Al ratios is the increased hydrophobicity of zeolite with the Si/Al ratio [8]. More Al-rich zeolites have a more hydrophilic micropore environment that favours inclusion and anchoring of Pd(II) as isolated sites (depending on proximity of Al atoms these Pd atoms exist either as Pd(II)/2Al or Pd(II)-OH/1Al).

We then tested these samples for catalytic methane combustion in the presence of steam under industrially relevant conditions at 390 °C and GHSV of ~150 L/g*hr. This is a representative temperature under which fast deactivation of various PdO samples has been previously demonstrated during vehicle operation, as mentioned in the introduction (Fig. 3).

For the sample containing atomically dispersed Pd in the micropores with Si/Al ~6, we observed almost no activity at this temperature. This is consistent with the presence of uniform redox inactive Pd(II)/2Al site [8,36]: such isolated cationic sites cannot activate oxygen and do not participate in methane combustion. The sample with small, poorly defined PdO nanoparticles on the external surface of SSZ-13 with Si/Al ratio of 12 has initial activity but deactivates with time-on-stream. Notably, PdO on SSZ-13 with Si/Al ratio of ~30 shows very little deactivation within the duration of the experiment (Fig. 3). We also tested PdO nanoparticles prepared by simple thermal decomposition of palladium nitrate precursor, which showed noticeable deactivation under the conditions studied. Deactivation was also observed for PdO/Al₂O₃ sample. Because in Pd/SSZ-13 sample with Si/Al ~20-30 all the activity comes from PdO on the external surface of

Pd/SSZ-13 samples, the difference in the deactivation behaviour of PdO should be due to the difference in surface sites.

Atomically resolved HAADF-STEM images of crystalline PdO nanoparticles on SSZ-13 with Si/Al ~20-30 were further analyzed

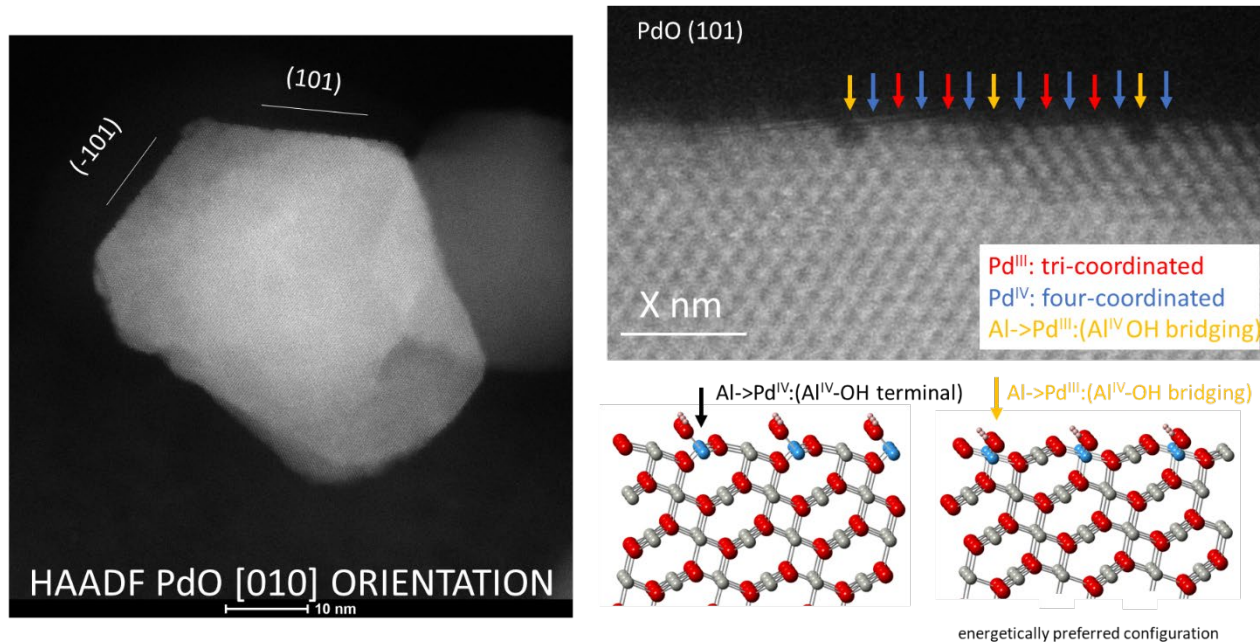


Figure 4. A) HAADF-STEM image of a typical PdO particle on SSZ-13 with Si/Al~30. B) Atomically resolved HAADF-STEM image of (101) facets of the image showing the presence of Al in place of missing Pd sites. Note that the missing Pd rows on (10-1) facet which equivalent with (101) are clearly shown in Fig. S4 C). Structural representation of the observed structure showing that Pd atoms (cations) are replaced by Al-OH sites specifically in Pd₁O₃ positions and not in Pd₁O₄ positions (based on the energies of calculated DFT structures).

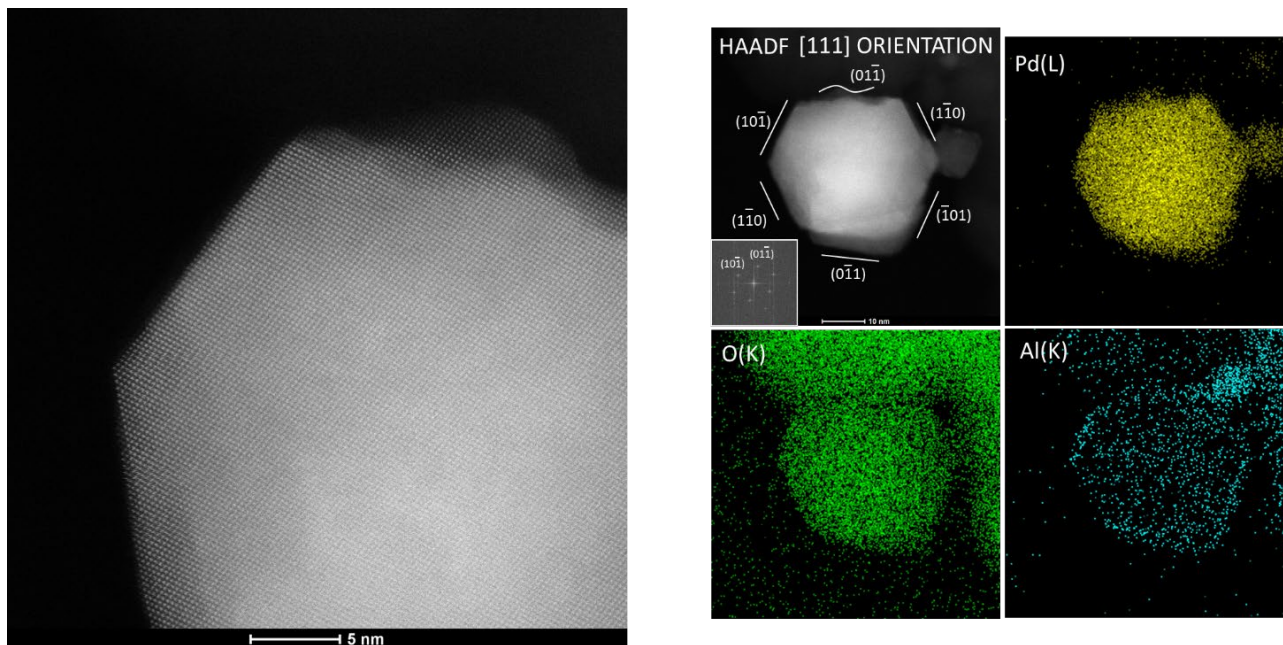


Figure 5. HAADF-STEM image of a typical well-faceted indexed PdO nanoparticle on SSZ-13 with Si/Al~30 and the corresponding EDS maps. The EDS maps show preferential enrichment with Al of the (101) facets of PdO.

(Fig. 4 and Figs. S4,S5 for additional images). Surprisingly, we could observe for the first time the presence of rows of missing Pd atoms present exclusively on (101) facets of PdO. Careful imaging of multiple nanoparticles in Pd/SSZ-13 Si/Al ~20-30 sample reveal this is a general phenomenon for (101) facets of PdO and we could not observe similar results for any other facets (confirmed by multiple HAADF-STEM images in Fig. S4, Fig S5 and Fig. S6). Our atomically resolved imaging shows (Fig. 4) that the missing rows are either a) tetrahedral Pd^{+2} atoms in $\text{Pd(II)}_4\text{O}_4$ adjacent to 3-coordinate $\text{Pd(II)}_3\text{O}_3$ sites as we mentioned earlier (such 3-coordinate Pd sites present on (101) facets are the ones responsible for the activation of methane), or b) tri-coordinate Pd atoms adjacent to 4-coordinate Pd_4O_4 sites.

The intensity present in the spots of missing Pd rows in (101) facet of PdO (Fig. 4) suggests that rows of some other element are incorporated into the structure. EDS mapping of the edges of PdO (Fig. 5, Fig. S7) unambiguously shows selective incorporation of Al^{+3} in place of Pd^{+2} atoms on (101) facets. It is important to note that in the atomically resolved image of PdO nanoparticle on which EDS was performed missing Pd was not clearly visible due to the orientation of this particle to the viewing plane (electron beam in Fig 5): the rows of missing Al atoms were located perpendicular to the imaging direction beyond the Pd atoms on the edge. Furthermore, we could not find rows of Al atoms incorporated into any other facets except (101) with careful HAADF-STEM imaging. To understand whether Al was incorporated into Pd_3O_3 or Pd_4O_4 site (only one scenario is possible), we performed DFT calculations (because the oxygen sub-lattice of PdO (101) cannot be directly imaged, it is not possible to conclude which specific Pd^{+2} site is occupied by Al^{+3} from the images although it is clear that only a) or b) is possible). For scenario a) Al would be incorporated as a pentahedral $\text{O}_4\text{Al(V)}\text{-OH}$ group. For scenario b) Al would be incorporated as a tetrahedral $\text{O}_3\text{Al(IV)}\text{-OH}$ group.

We performed DFT calculations on PdO (101) to determine which scenario is operative (Fig. 6). We find that incorporation of

$\text{O}_3\text{Al}^{+3}\text{(IV)}\text{-OH}$ moiety in place of $\text{Pd}^{+2}_3\text{O}_3$ site (scenario b) is >1 eV more favourable than scenario a). Thus, we can conclude that atom-thin rows of $\text{O}_3\text{Al(IV)}\text{-OH}$ occupy the spots of Pd_3O_3 directly adjacent to Pd_4O_4 sites – the former being crucial for methane activation.

When PdO forms and assembles from decomposition of a nitrate precursor without the presence of mobile Al species, no incorporation of Al would take place as expected. Countless previous images of supported and unsupported PdO nanoparticles (and oriented films) have never observed or suggested incorporation of any other species in (101) facets. Even for PdO formation on the typically used gamma-alumina surface this does not occur – the reason for this lies in the stability of gamma-alumina surface and its “unwillingness” to release any Al species which is well known [38-40].

However, only when PdO self-assembly takes place from the deposited nitrate precursor on zeolite SSZ-13, this phenomenon does occur. Solid-state ^{27}Al NMR data for Pd/SSZ-13 system confirms this finding (Fig. S8): more specifically, we observed that highly mobile Al-aqua complexes are present in the sample (formed from Al diffusion from the bulk of SSZ-13 crystals) (Fig. S7). The mobility of these ions is evident due to the sharpness of ^{27}Al NMR feature [41,42]. Thus, mobile Al ions, released in small amounts by zeolite with low amounts of Al (siliceous zeolite), get incorporated into the surface of PdO during PdO self-assembly process. DFT calculations show (Fig. 6) the favourability of the incorporation of rows of $\text{O}_3\text{Al}^{+3}\text{(IV)}\text{-OH}$ moieties that insert into the surface in place of Pd_3O_3 specifically sitting next to $\text{Pd}^{+2}_4\text{O}_4$. This

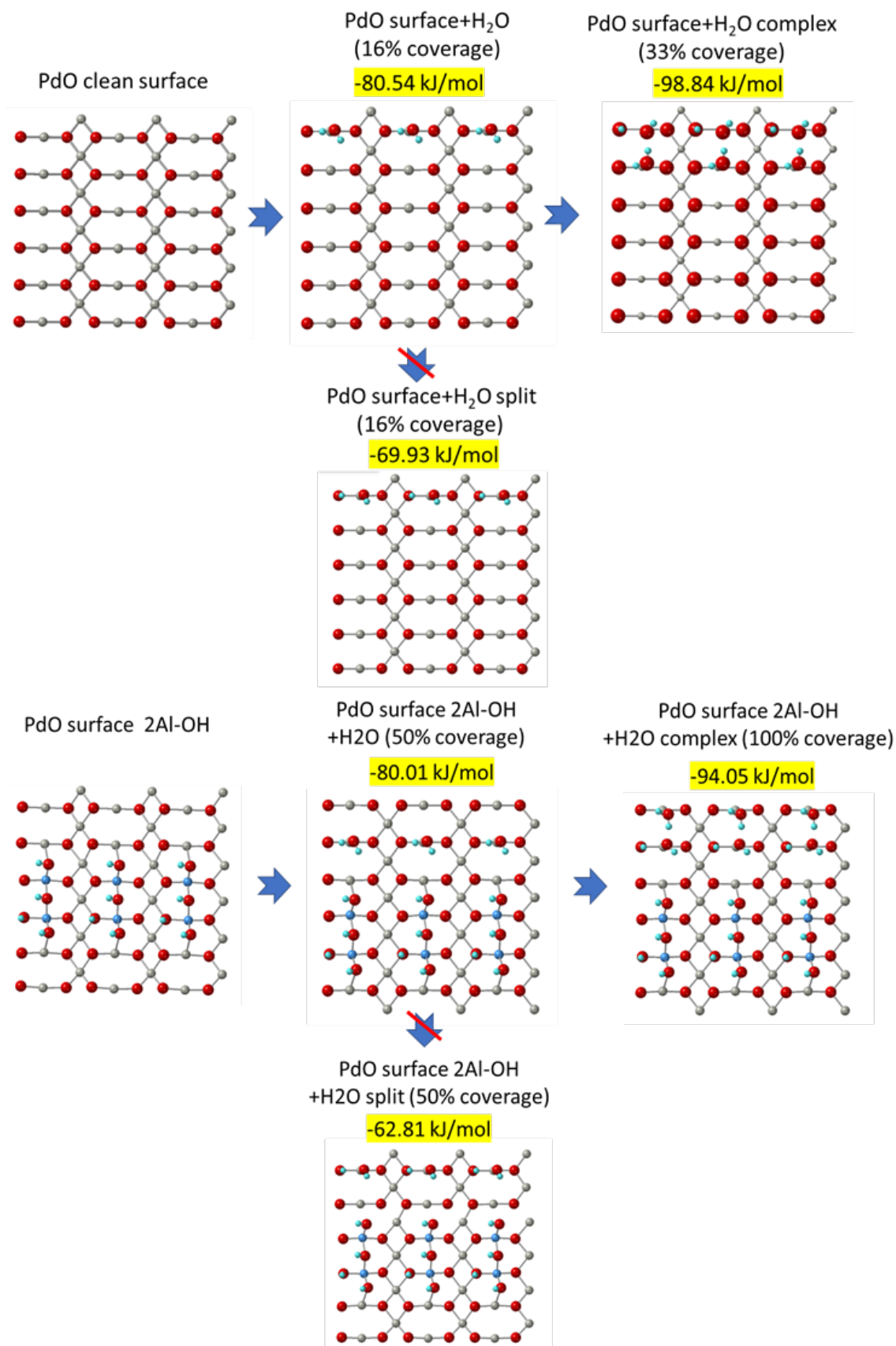


Figure 6. DFT calculations showing: (101) facet of PdO clean surface interacting with water (at different coverages) (top graph) and (101) facet of PdO surface incorporating two adjacent Al-OH groups in place of two PdO sites and interacting with water molecules (bottom graph).

indicates that the presence of such atomically thin rows of Al-OH moieties adjacent to Pd₄O₄ prevents deactivation by water. We turned to DFT calculations to help us understand the poisoning effect of water on Pd₄O₃ sites (Fig. 6). On the undoped (101) PdO surface, water adsorption on O₃Pd(IV)-OH site (with a bridging proton forming simultaneously) is favourable. Surprisingly, we found that dissociation of only one water molecule on (101) PdO is energetically unfavourable (Fig. 6) compared to undissociated water molecule, which is in agreement with pioneering studies by Weaver and co-workers [25-32]. The dissociated state is higher by 11 kJ/mol-Pd than the undissociated one. However, we discovered that in presence of nearby H₂O molecules on Pd_{tri}, chemisorbed near the dissociated H₂O molecules on the adjacent Pd_{tri} site, leads to the extremely stable configuration with ~30 kJ/mol-Pd energy gain. Thus, the presence of H₂O dimers (and trimers) on the surface with one H₂O molecule dissociated and 1 undissociated on the adjacent Pd_{tri} site is responsible for the water poisoning effect.

To understand this, we performed the DFT calculations on the surface containing adjacent Al atoms replacing Pd_{tri} sites on (101) facet (Fig. 6). Our findings show that although some minor decrease of water dissociation is observed (~4 kJ/mol-Pd), it is too minor to account for the observed effect. Thus, we infer that Al incorporation into (101) facets of PdO instead of Pd_{tri} kinetically destabilizes water dissociation by disrupting the formation of extremely stable H₂O dimers and trimers (with 1 H₂O dissociated) on adjacent Pd_{tri} sites.

These findings, based on combined state-of-the-art spectroscopic, microscopic, theoretical and catalytic approach reveal a previously unattainable insight into structure-catalytic property relationships of industrially used PdO catalysts, and highlight a new strategy of developing an important class of catalytical materials with water-tolerance on the basis of the facet-selective heterometal doping approach.

Acknowledgements

The research at PNNL was supported by the U.S. Department of Energy, Energy Efficiency and Renewable Energy, Vehicle Technology Office. Experiments were conducted in the Environmental Molecular Sciences Laboratory (EMSL), a national scientific user facility sponsored by the Department of Energy's Office of Biological and Environmental Research at Pacific Northwest National Laboratory (PNNL). PNNL is a multi-program national laboratory operated for the DOE by Battelle Memorial Institute under Contract DE-AC06-76RL01830. We acknowledge the support of CLEERS (Crosscut Lean Exhaust Emissions Reduction Simulations). CLEERS is an initiative funded by the U.S. Department of Energy (DOE) Vehicle Technologies Office to support the development of accurate tools for use in the design, calibration, and control of next generation engine/emissions control systems that maximize efficiency while complying with emissions regulations.

*Corresponding authors.

† These authors contributed equally.

Conflict of interest

No conflicts to declare.

Keywords: Palladium Oxide nanoparticles; Methane combustion; Palladium oxide supported on siliceous SSZ-13 zeolite; HAADF-STEM imaging; Facet specific heteroatom doping;

- (1) Royal College of Paediatrics and Child Health. Every breath we take—the lifelong impact of air pollution. London: Royal College of Paediatrics and Child Health, 2016.
- (2) N. R. Jaegers, J. K. Lai, Y. He, E. Walter, D. A. Dixon, M. Vasilu, Y. Chen, C. M. Wang, M. Y. Hu, K. T. Mueller, I. E. Wachs, Y. Wang and J. Z. Hu, *Angew. Chem., Int. Ed.*, 2019, 131, 12739–12746.
- (3) Ja-Hun Kwak, Russell G Tonkyn, Do Heui Kim, János Szanyi, Charles HF Peden, *J. Catal.*, 2010, 275, 187-190.
- (4) I. Bull, A. Moini, G. Koerner, J. Patchett, W. Jaglowski, S. Roth, US Patent US20070134146A1, 2010.
- (5) Zones, S.I. US Patent 4 544 538, 1985.
- (6) T. Seiyama, T. Arakawa, T. Matsuda, N. Yamazoe, and Y. Takita, *Chem. Lett.*, 781 (1975)
- (7) Chen, H.-Y.; Collier, J. E.; Liu, D.; Mantarosi, L.; Durán- Martín, D.; Novák, V.; Rajaram, R. R.; Thompsett, D. *Catal. Lett.* 2016, 146 (9), 1706–1711.
- (8) Khivantsev, K.; Jaegers, N. R.; Kovarik, L.; Hanson, J. C.; Tao, F. (Feng); Tang, Y.; Zhang, X.; Koleva, I. Z.; Aleksandrov, H. A.; Vayssilov, G. N.; Wang, Y.; Gao, F.; Szanyi, J. *Angew. Chem.* 2018, 130 (51), 16914–16919.
- (9) Twigg, M.V., Haren Gandhi 1941-2010: Contributions to the Development and Implementation of Catalytic Emissions Control Systems. *Platinum Metals Review*, 2011. 55(1): p. 43-53.
- (10) Warlimont, H.; W.E. Martienssen, eds. *Springer Handbook of Condensed Matter and Materials Data*. 2006.
- (11) Mouadib, N.; Feumijantou, C.; Garbowski, E.; Primet, M., *Appl Catal a-Gen* **1992**, 87 (1), 129-144.
- (12) Gelin, P.; Primet, M., *Appl Catal B-Environ* **2002**, 39 (1), 1-37.
- (13) Eguchi, K.; Arai, H., *Catal Today* **1996**, 29 (1-4), 379-386.
- (14) Choudhary, T. V.; Banerjee, S.; Choudhary, V. R., *Appl Catal a-Gen* **2002**, 234 (1-2), 1-23.
- (15) Cullis, C. F.; Willatt, B. M., *J Catal* **1983**, 83 (2), 267-285.
- (16) Lyubovskiy, M.; Pfefferle, L., *Catal Today* **1999**, 47 (1-4), 29-44.
- (17) Eguchi, K.; Arai, H., *Appl Catal a-Gen* **2001**, 222 (1-2), 359-367.
- (18) Ciuparu, D.; Lyubovskiy, M. R.; Altman, E.; Pfefferle, L. D.; Datye, A., *Catal Rev* **2002**, 44 (4), 593-649.
- (19) Lampert, J. K.; Kazi, M. S.; Farrauto, R. J., *Appl Catal B-Environ* **1997**, 14 (3-4), 211-223.
- (20) Sekizawa, K.; Widjaja, H.; Maeda, S.; Ozawa, Y.; Eguchi, K., *Catal Today* **2000**, 59 (1-2), 69-74.
- (21) Chin, Y.-H.; García-Diéguez, M. n.; Iglesia, E., *The Journal of Physical Chemistry C* 2016, 120 (3), 1446-1460.
- (22) Chin, Y.-H.; Iglesia, E., *The Journal of Physical Chemistry C* 2011, 115 (36), 17845-17855.
- (23) Fujimoto, K.-i.; Ribeiro, F. H.; Avalos-Borja, M.; Iglesia, E., *Journal of Catalysis* 1998, 179 (2), 431-442.
- (24) Chin, Y.-H.; Buda, C.; Neurock, M.; Iglesia, E., *Journal of the American Chemical Society* 2013, 135 (41), 15425-15442.
- (25) Martin, N. M.; Van den Bossche, M.; Hellman, A.; Gronbeck, H.; Hakanoglu, C.; Gustafson, J.; Blomberg, S.; Johansson, N.; Liu, Z.; Axnanda, S.; Weaver, J. F.; Lundgren, E., *ACS Catalysis* 2014, 4 (10), 3330-3334.
- (26) Weaver, J. F.; Hinojosa, J. A., Jr.; Hakanoglu, C.; Antony, A.; Hawkins, J. M.; Asthagiri, A. *Catal. Today* 2011, 160, 213
- (27) Bossche, M. V.; Gronbeck, H. *J. Am. Chem. Soc.* 2015, 137 (37), 12035–12044.

- (28) Hellman, A.; Resta, A.; Martin, N. M.; Gustafson, J.; Trincherro, A.; Carlsson, P.-A.; Balmes, O.; Felici, R.; van Rijn, R.; Frenken, J. W. M.; Andersen, J. N.; Lundgren, E.; Grönbeck, H. *Phys. Chem. Lett.* 2012, 3, 678
- (29) Weaver, J. F.; Hakanoglu, C.; Antony, A. & Asthagiri, A. *Chem. Soc. Rev.* 43, 7536–7547 (2014).
- (30) Antony, A., Asthagiri, A. & Weaver, J. F. *J. Chem. Phys.* 139, 104702 (2013).
- (31) Zhang F, Pan L, Choi J, Mehar V, Diulus JT, Asthagiri A, Weaver JF (2015) *Angew Chem Int Ed Engl* 54(47):13907–13911
- (32) Weaver, J. F.; Hakanoglu, C.; Hawkins, J. M.; Asthagiri, A. *J. Chem. Phys.* 2010, 132, No. 024709.
- (33) K. Okumura, E. Shinohara, M. Niwa, *Catal. Today*, 117 (2006), pp. 577-583
- (34) J. Lim, D. Jo, S. Hong, *Appl. Catal. B Environ.*, 219 (2017), pp. 155-162
- (35) Y. Luo, H.H. Funke, J.L. Falconer, R.D. Noble, *Ind. Eng. Chem. Res.*, 55 (2016), pp. 9749-9757
- (36) Khivantsev, K.; Jaegers, N. R.; Koleva, I. Z.; Aleksandrov, H. A.; Kovarik, L.; Engelhard, M.; Gao, F.; Wang, Y.; Vayssilov, G. N.; Szanyi, J. *J. Phys. Chem. C* 2020, 124 (1), 309–321.
- (37) Jaegers, N. R.; Khivantsev, K.; Kovarik, L.; Klas, D. W.; Hu, J. Z.; Wang, Y.; Szanyi, J. *Catal. Sci. Technol.* 2019, 9, 6570–6576.
- (38) L. Kovarik, A. Genc, C. Wang, A. Qiu, C.H. Peden, J. Szanyi, J.H. Kwak, *The Journal of Physical Chemistry C*, 117 (2013) 179-186
- (39) L. Kovarik, M. Bowden, A. Andersen, N. R. Jaegers, N. Washton, J. Szanyi, *Chemrxiv* 2020 DOI: 10.26434/chemrxiv.12584783.v1
- (40) K. Khivantsev, N. R. Jaegers, J.-H. Kwak, J. Szanyi, L. Kovarik, *Chemrxiv* 2020 DOI: 10.26434/chemrxiv.11829576
- (41) Wang, M.; Jaegers, N. R.; Lee, M. S.; Wan, C.; Hu, J. Z.; Shi, H.; Mei, D. H.; Burton, S. D.; Camaioni, D. M.; Gutierrez, O. Y.; Lercher, J. J. *Am. Chem. Soc.* 2019, 141, 3444–3455
- (42) Khivantsev, K.; Jaegers, N. R.; Kovarik, L.; Proding, S.; Derewinski, M. A.; Wang, Y.; Gao, F.; Szanyi, J. *Appl. Catal. A. Gen.* 2019, 569, 141–148.

Supporting Information

PdO self-assembly on zeolite SSZ-13 with rows of $\text{O}_3\text{Al}^{+3}(\text{IV})\text{OH}_{\text{bridging}}$ selectively incorporated in PdO(101) facets for moisture-resistant methane oxidation

Libor Kovarik,^{a†*} Nicholas R. Jaegers,^a Janos Szanyi,^{a*} Miroslaw A. Derewinski,^{a,b} Yong Wang^{a,c*} and Konstantin Khivantsev^{a†*}

^aInstitute for Integrated Catalysis, Pacific Northwest National Laboratory Richland, WA 99352 USA

^bJerzy Haber Institute of Catalysis and Surface Chemistry Polish Academy of Sciences, Krakow, Poland PL-30239

^cVoiland School of Chemical Engineering and Bioengineering, Washington State University, Pullman, WA 99163 USA

METHODS

Na-SSZ-13 with Si/Al ~ 6, 10-12 and 20-30 was hydrothermally synthesized using the following recipe: 0.8 g of NaOH (Sigma Aldrich, $\geq 99\%$) was dissolved in 50 ml of deionized water. Then, 17 g of TMAO-H (Sachem Inc., 25% N,N,N-trimethyl-1-adamantyl ammonium hydroxide) was added as structure directing agent. Consequently, 1.5 g (or 0.75g, or 0.3g, depending on the desired amount of Al in the framework) of $\text{Al}(\text{OH})_3$ (Sigma Aldrich, $\sim 54\% \text{Al}_2\text{O}_3$) was slowly added to the solution and stirred at 400 rpm until it was completely dissolved. Afterwards, 20.0 g of LUDOX HS-30 colloidal silica (Sigma Aldrich, 30 wt% suspension in H_2O) was added slowly to the solution until a uniform white gel was formed. The obtained gel was sealed in a 125 mL Teflon-lined stainless-steel autoclave containing a magnetic stir bar. Hydrothermal synthesis was carried out at 160 °C under continuous gel stirring at 400 rpm for 4 days. After synthesis, the zeolite cake was separated from the suspension by centrifugation and washed with deionized water. It was afterwards dried at 80 °C under N_2 flow overnight and calcined in air at 600 °C for 5 h in order to remove the SDA. The as-obtained Na-SSZ-13 samples with varying Si/Al ratios were ion-exchanged twice with 2 M NH_4NO_3 aqueous solution at 80 °C for 3 hours yielding the ammonium forms of SSZ-13. NH_4 -SSZ-13 was subsequently dried under ambient conditions and then at 80 °C.

Samples with 1 wt% Pd were prepared via the following method: minimum amount of the $[\text{Pd}(\text{II})(\text{NH}_3)_4](\text{NO}_3)_2$ precursor solution was added to zeolite in the amount approximately equivalent to the total pore volume of the zeolite. The thick paste was mixed vigorously for 30 minutes, followed by calcination in air at 650 °C for 5 h (ramping rate 2 °C/min).

Sample with 1wt% Pd on SBA-200 gamma-alumina (CATALOX, high-purity gamma-alumina) was prepared in an identical fashion as for zeolites and calcined in air 650 °C for 5 h (ramping rate 2 °C/min).

Palladium oxide nanoparticles were prepared by decomposing palladium tetramine nitrate in the air flow at 600 °C for 3 hours. For catalytic experiments, ~ 1.3 mg of PdO was mixed with 120 mg of pre-calcined low-surface area high-purity alpha-alumina.

Methane combustion experiments were carried out in a quartz plug-flow reactor. The gas feed contained 850 ppm CH_4 , 13% O_2 and $\sim 3\%$ H_2O balanced with N_2 . The total flow was adjusted to 300 sscm/min. Gas concentrations were continuously monitored with an online MKS

MultiGasTM 2030 FTIR gas analyzer with the gas cell maintained at 191 °C. 120 mg of catalyst was loaded and tests were conducted at 390 °C. The catalysts were first exposed to the dry air for at the desired temperature for ~ 1 hours, then to reactants at 390 °C for 15 minutes for stabilization. Methane conversion curves vs time-on-stream were collected immediately afterwards and are reported in the main text.

The in situ static transmission IR experiments were conducted in a home-built cell housed in the sample compartment of a Bruker Vertex 80 spectrometer, equipped with an MCT detector and operated at 4 cm⁻¹ resolution. The powder sample was pressed onto a tungsten mesh which, in turn, was mounted onto a copper heating assembly attached to a ceramic feedthrough. The sample could be resistively heated, and the sample temperature was monitored by a thermocouple spot welded onto the top center of the W grid. The cold finger on the glass bulb containing CO was cooled with liquid nitrogen to eliminate any contamination originating from metal carbonyls. Prior to spectrum collection, a background with the activated (pre-oxidized) sample in the IR beam was collected. Each spectrum reported is obtained by averaging 256 scans.

HAADF-STEM was used to probe the dispersion of Pd in prepared samples as well as provide imaging of PdO at the atomic level. The analysis was performed with probe corrected Thermo Fisher Titan 80-300 and Themis Z 30-300 microscopes operated at 300 kV. Both microscopes are equipped with CEOS GmbH double-hexapole aberration corrector for the probe-forming lens. Images obtained with Titan were acquired with annular dark field (HAADF) detector, using a convergence angle of 18 mrad and the inner collection angle of 52 mrad. Compositional analysis was performed with EDS, using an Oxford X-Max^N100TLE solid drift detector SDD (100 mm²). The EDS data collection and processing was performed with Oxford's Aztec software package. Images obtained with Themis Z were acquired with annular dark field (HAADF) using convergence angle of either 19 or 26 mrad and the inner collection angle of 48 mrad. The EDS data were collected with Thermo Fisher Super-X Detection System and Velox software package.

Cryo High-energy X-ray Diffraction (XRD) data were collected at beamline 11-ID-B at the Advanced Photon Source at Argonne National Laboratory using 58.6 keV (0.2114 Å) X-rays. Samples were loaded in the powder form in low-background Kapton capillary holders, and cooled using liquid nitrogen microjets. Data were collected using amorphous silicon-based area detectors.

Geometric corrections and reduction to one-dimensional data used GSAS-II. ^{27}Al MAS NMR measurements were performed at room temperature on a Bruker 850 MHz NMR spectrometer, operating at a magnetic field of 19.975 T. The corresponding ^{27}Al Larmor frequency is 221.412598 MHz. All spectra were acquired at a sample spinning rate of 18.7 kHz (± 5 Hz) and externally referenced to 1.0 M aqueous $\text{Al}(\text{NO}_3)_3$ (0 ppm). The advantages of both enhanced spectral resolution and sensitivity for acquiring ^{27}Al MAS NMR at ultrahigh field (19.975 T) have been established previously.

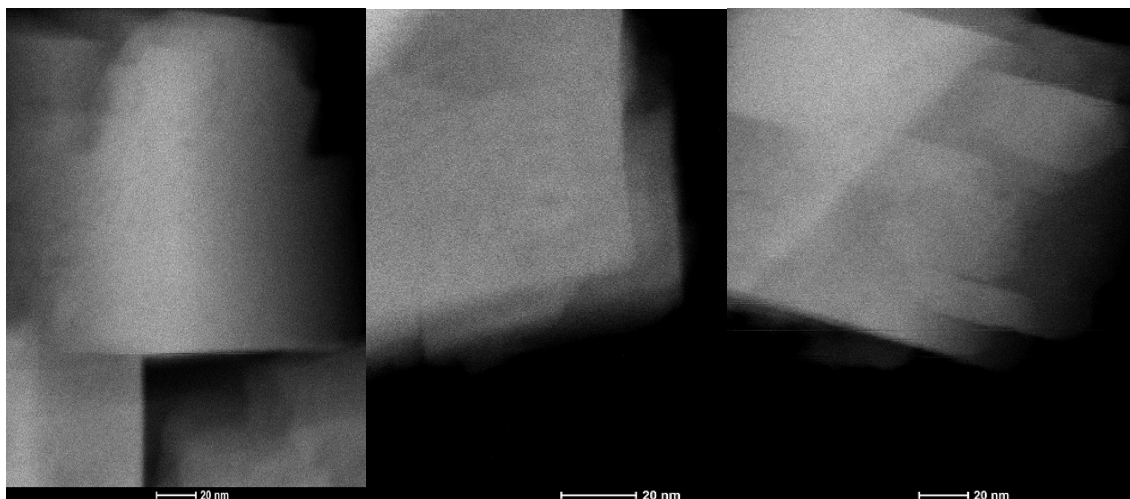


Figure S1. Additional HAADF-STEM images of 1 wt% Pd/SSZ13 with Si/Al ratio 6.

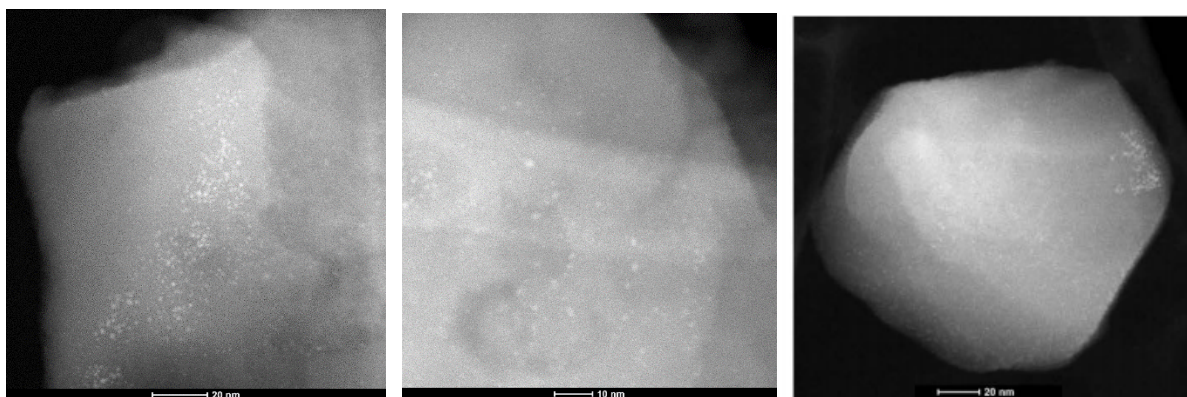


Figure S2. Additional HAADF-STEM images of 1 wt% Pd/SSZ13 with Si/Al ratio 12.

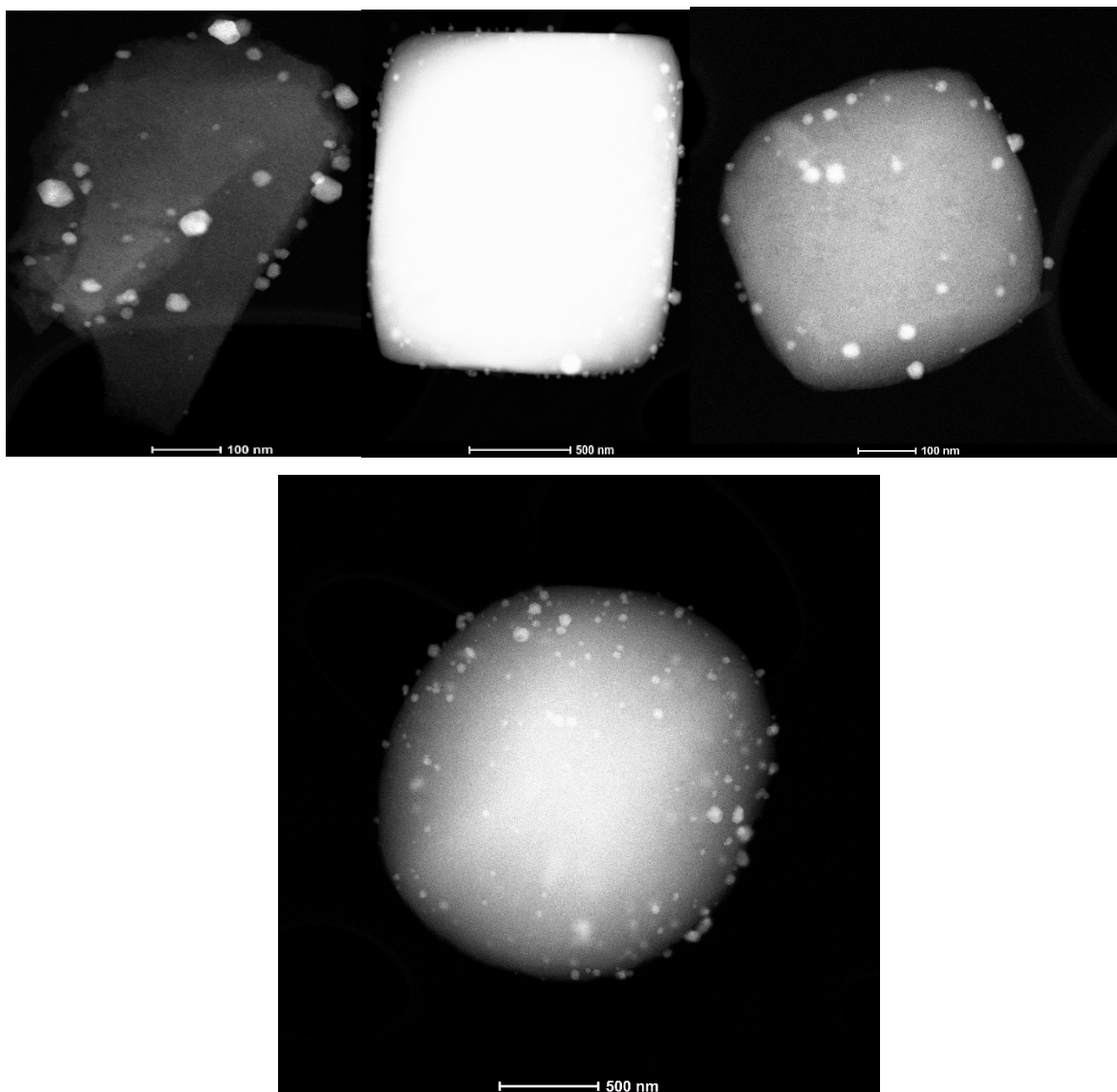
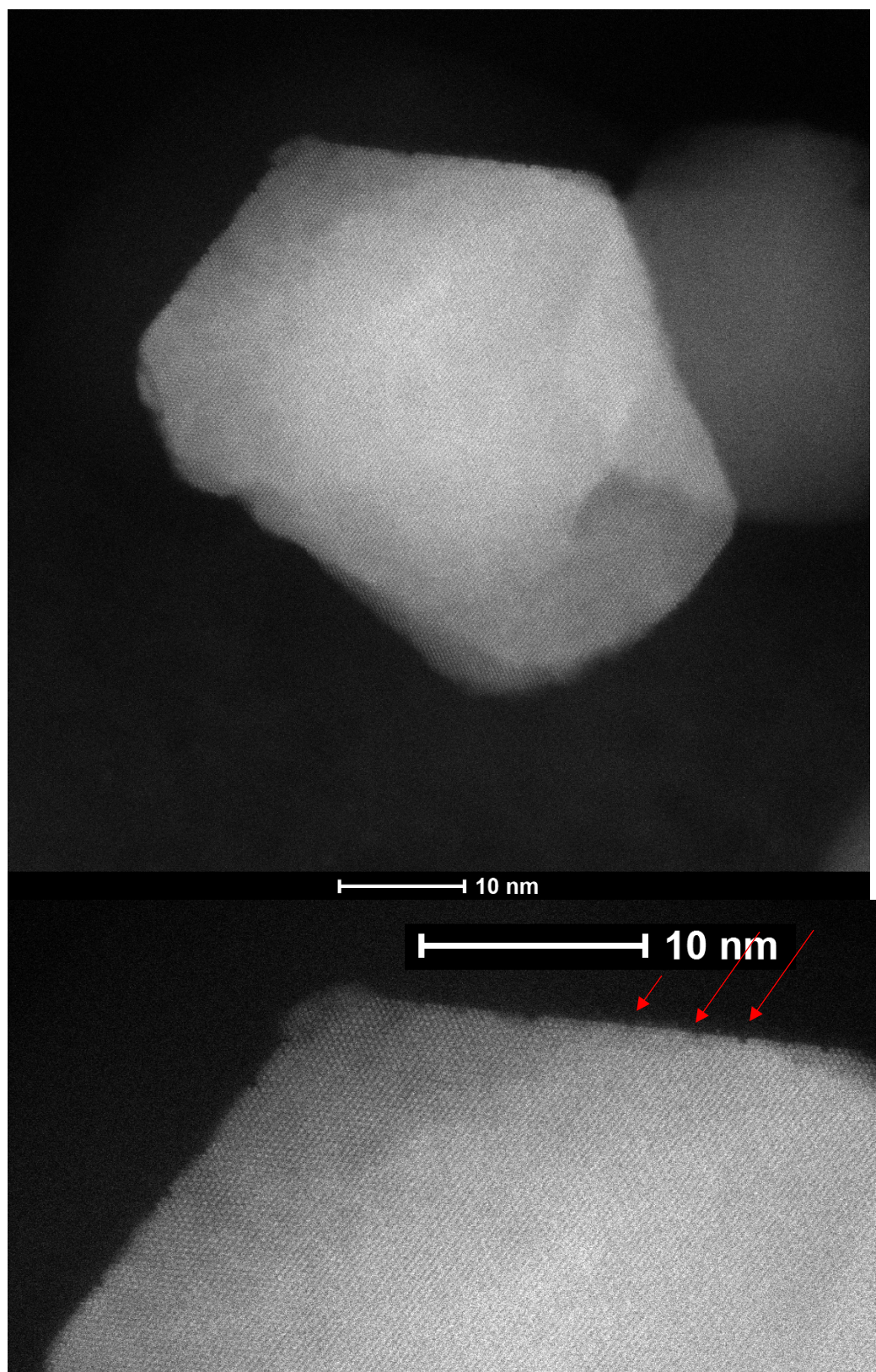
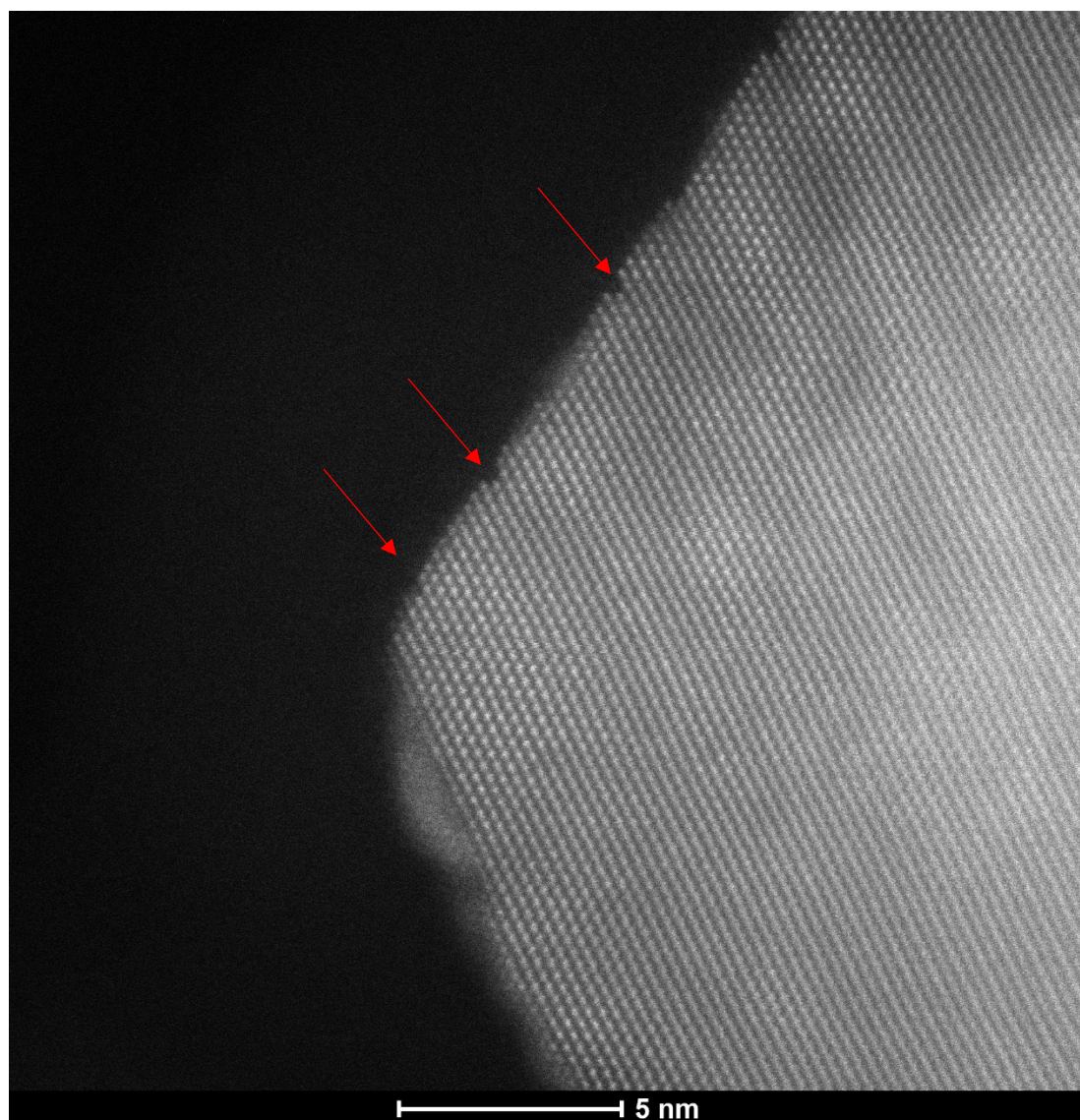


Figure S3. Additional HAADF-STEM images of 1 wt% Pd/SSZ13 with Si/Al ratio 30.





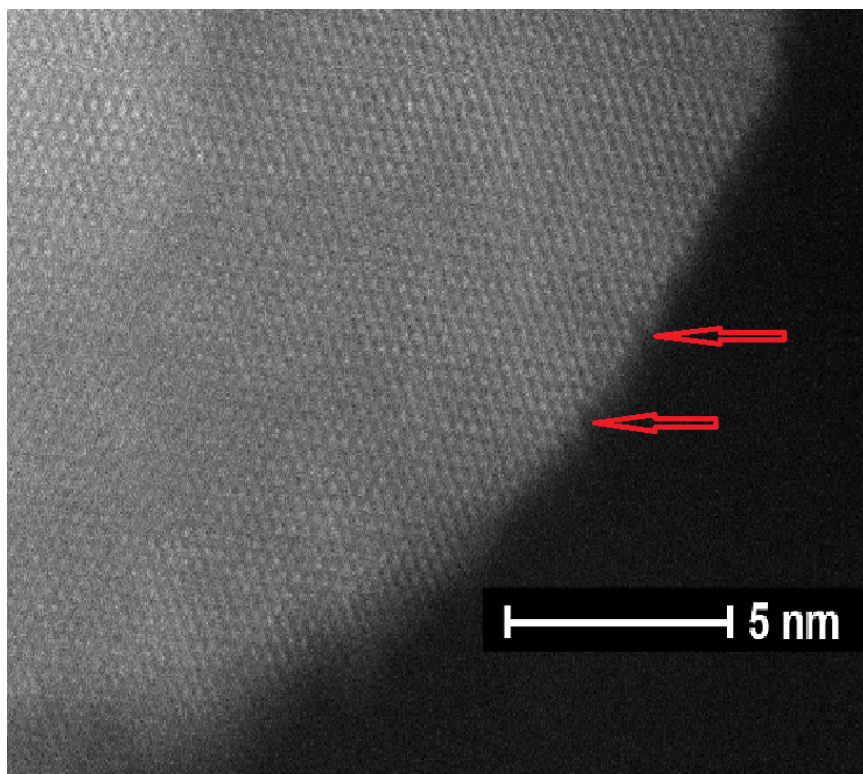
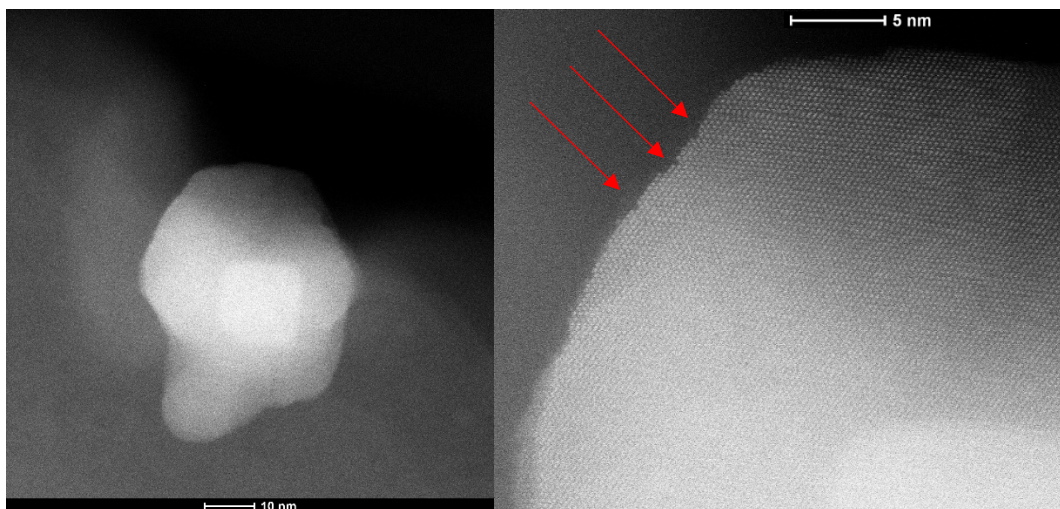


Figure S4. HAADF-STEM images (of different magnification) of a faceted PdO crystal on 1 wt% Pd/SSZ13 with Si/Al ratio ~20-30 showing presence of rows of “missing” Pd atoms exclusively on (101) facets.



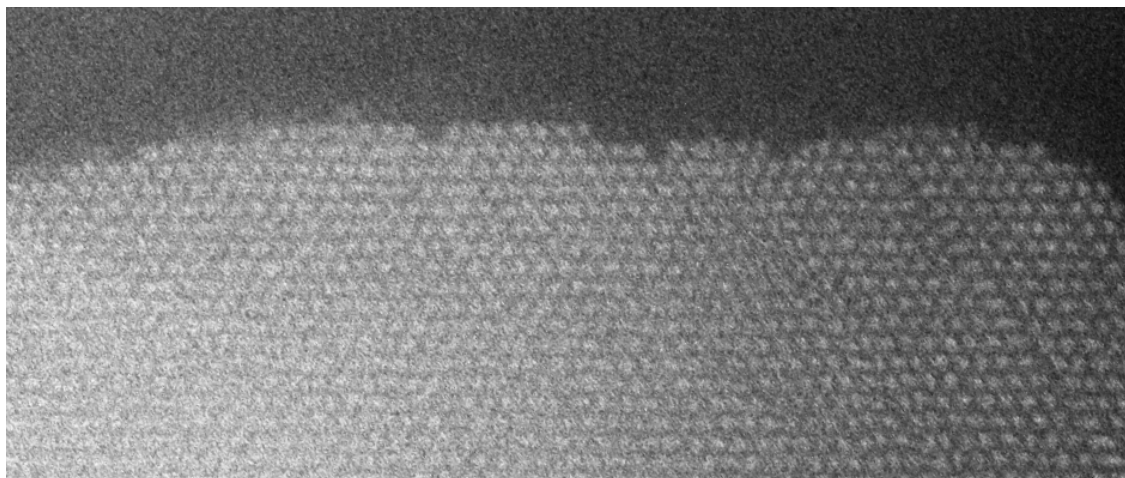
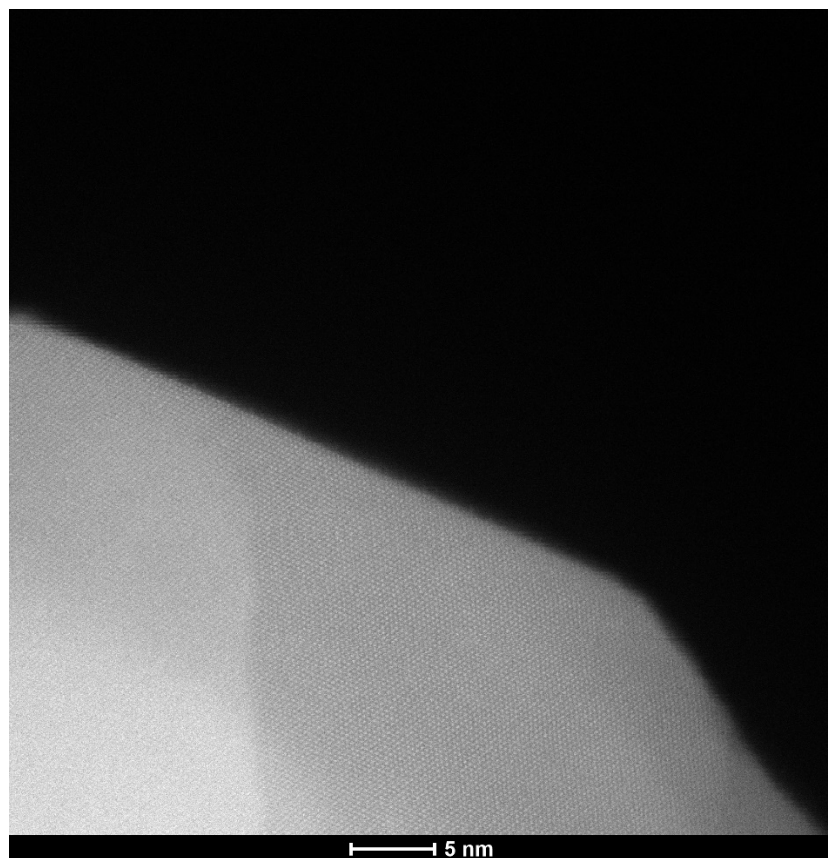
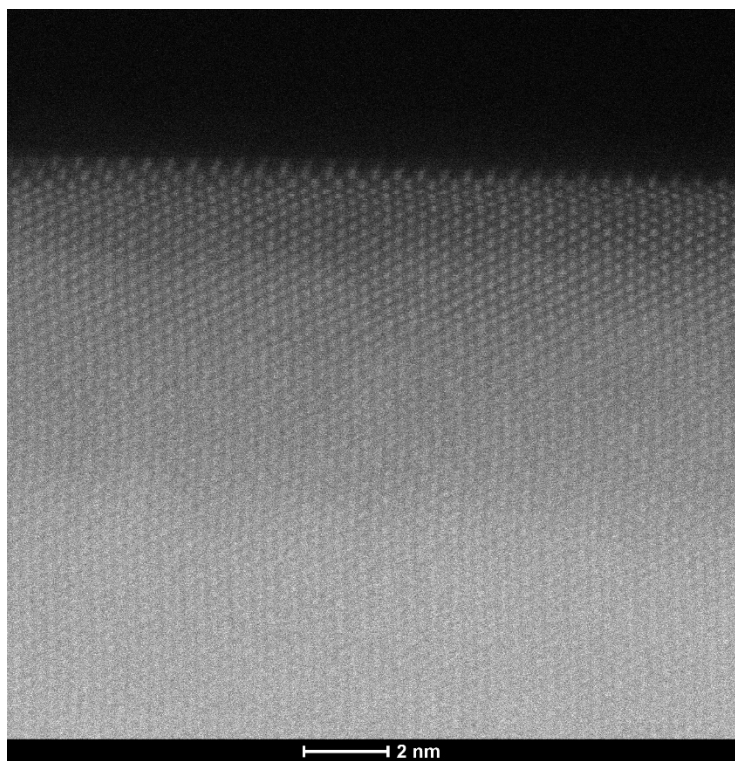


Figure S5. HAADF-STEM images of another faceted PdO crystal on 1 wt% Pd/SSZ13 with Si/Al ratio ~20-30, showing rows of “missing” Pd atoms on (101) facet.





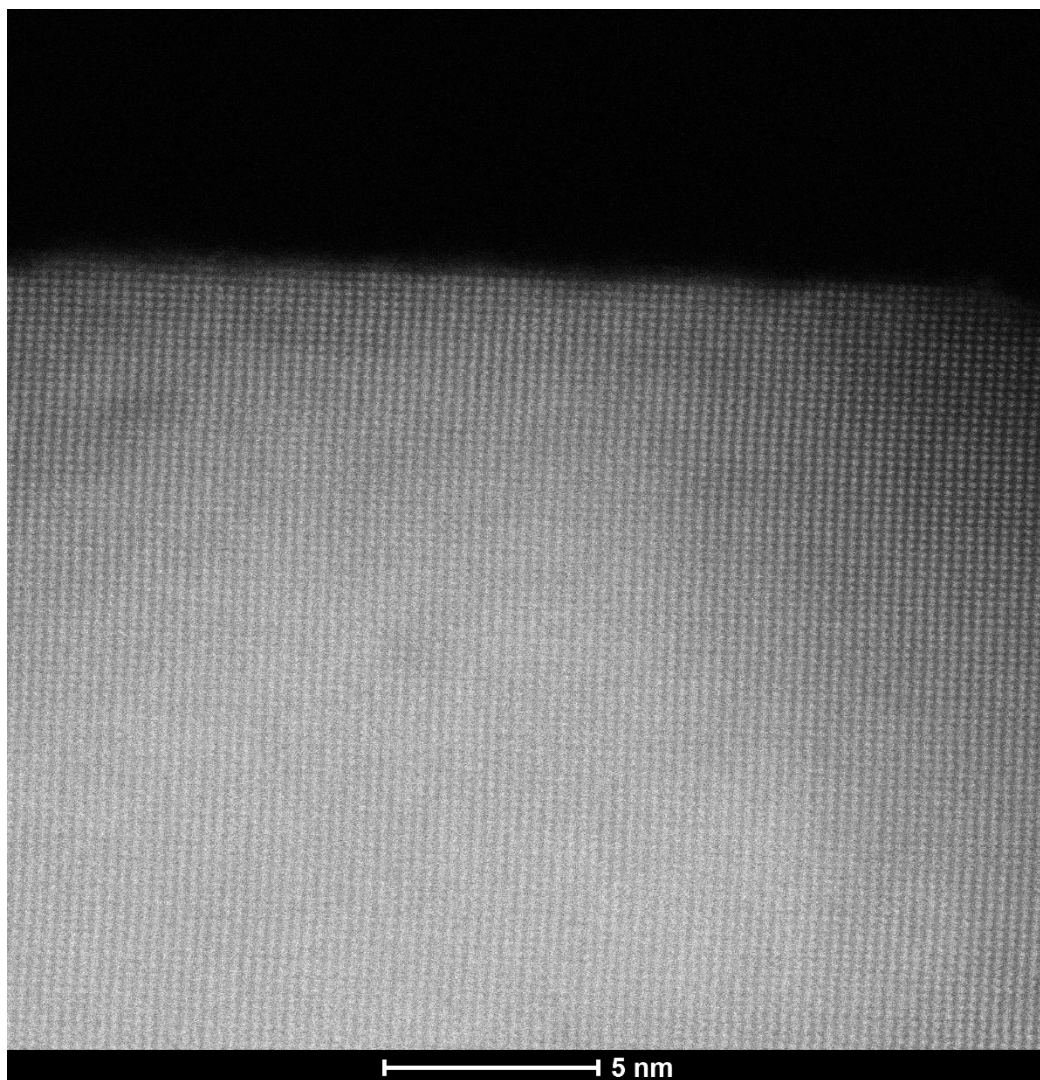


Figure S6. Additional HAADF-STEM images of non-(101) PdO facets on 1 wt%Pd/SSZ-13 with Si/Al \sim 20-30, showing lack of missing rows of Pd atoms.

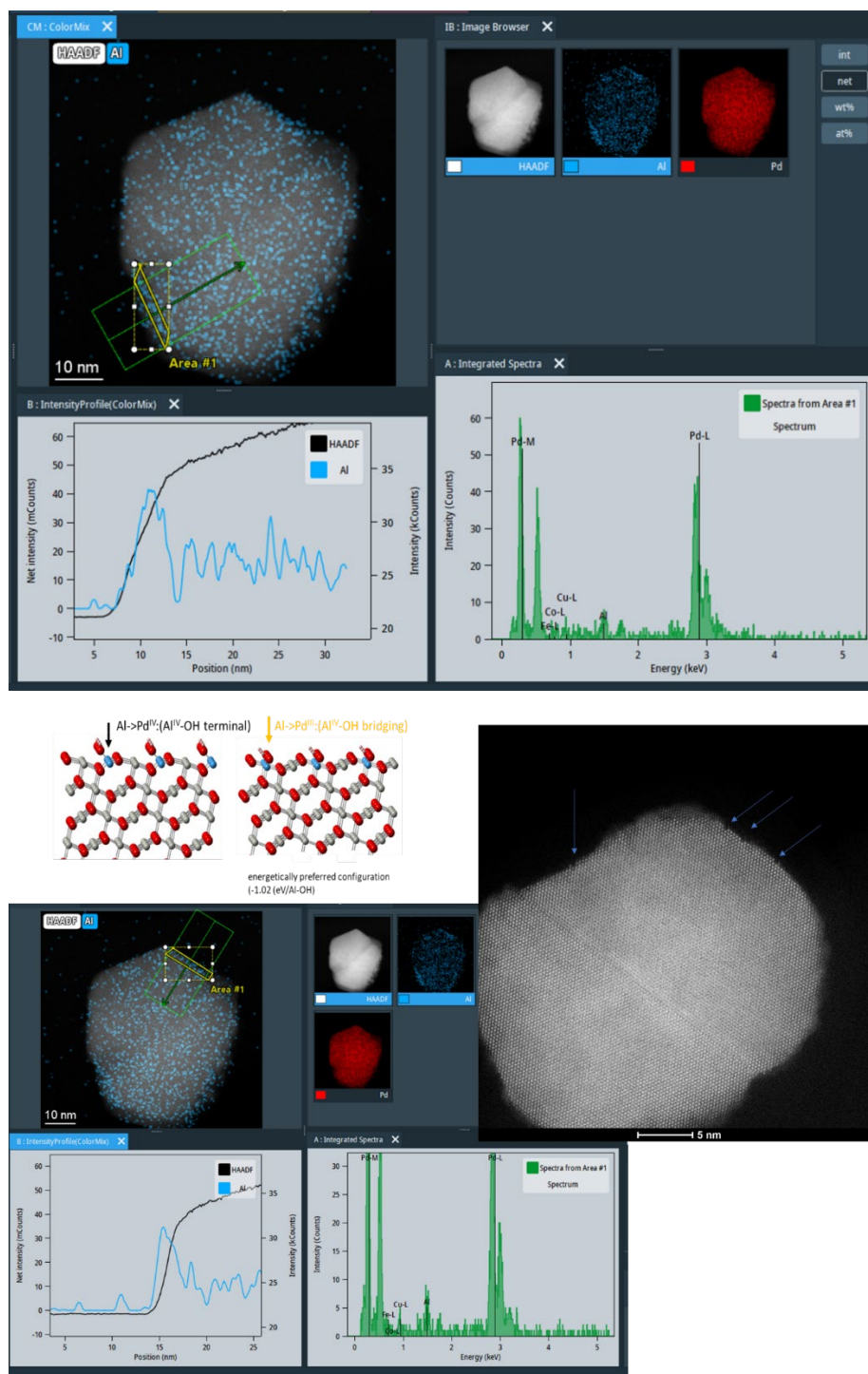


Fig. S7. Atomically resolved HAADF-STEM images of a well-faceted PdO nanoparticle on the surface of SSZ-13 zeolite. Missing rows of Pd atoms are identified on (101) facets. EDS maps reveal incorporation of Al at the edges of PdO particles. Corresponding DFT calculations show that incorporation of Al-OH in place of Pd tri-coordinate sites is significantly more favourable than Pd tetra-coordinate sites.

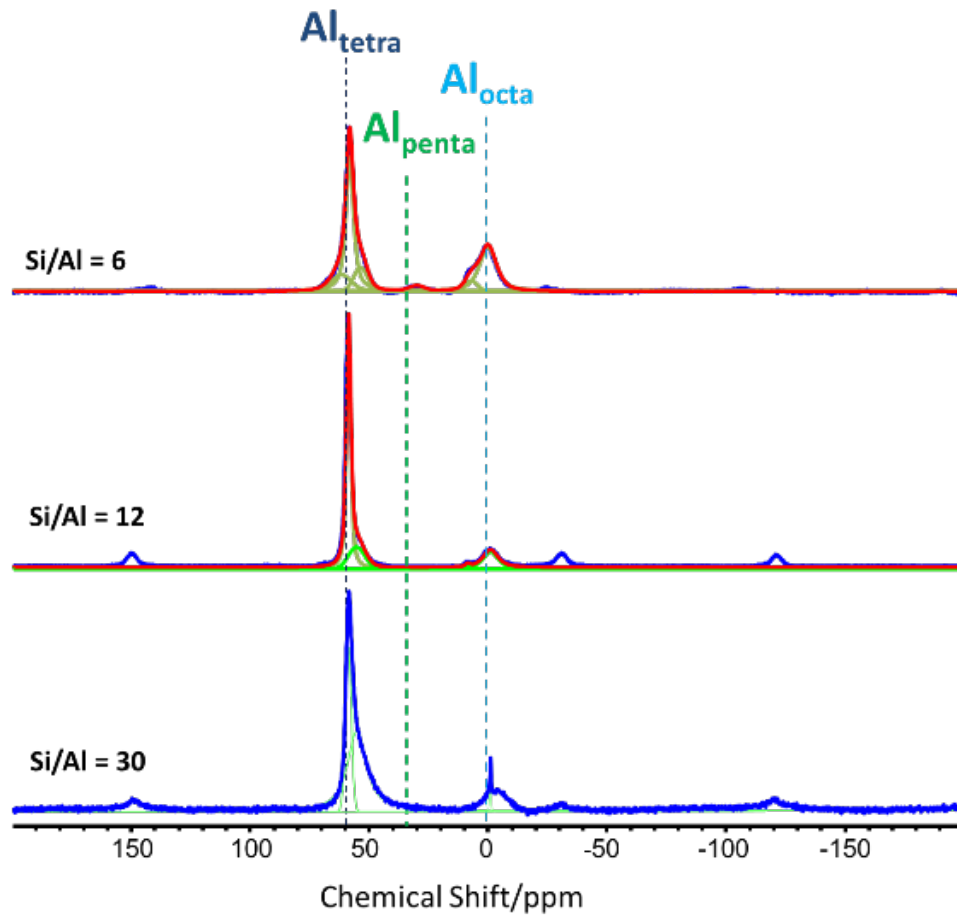


Figure S8. ^{27}Al high-field solid state NMR on 1 wt% Pd/SSZ-13 with Si/Al ratio 6, 12 and 30 respectively. Sharp signal at ~ 0 ppm corresponds to mobile Al species.